J|A|C|S

JOURNAL OF THE AMERICAN CHEMICAL SOCIETY

Article

pubs.acs.org/JACS

Photoactivation Mechanism, Timing of Protein Secondary Structure Dynamics and Carotenoid Translocation in the Orange Carotenoid Protein

Patrick E. Konold,[†] Ivo H. M. van Stokkum,[†] Fernando Muzzopappa,[‡,¶] Adjélé Wilson,[‡,¶] Marie-Louise Groot,[†] Diana Kirilovsky,[‡,¶] and John T. M. Kennis*[,†]

[†]Department of Physics and Astronomy, Faculty of Sciences, Vrije Universiteit, De Boelelaan 1081, 1081HV Amsterdam, The Netherlands

[‡]Institute for Integrative Biology of the Cell (I2BC), CEA, CNRS, Universite Paris-Sud, Universite Paris-Saclay, 91198 Gif-sur-Yvette, France

[¶]Institut Joliot, Commissariat a l'Energie Atomique (CEA), 91191 Gif-sur-Yvette, France

Ⓢ *Supporting Information*

ABSTRACT: The orange carotenoid protein (OCP) is a two-domain photoactive protein that noncovalently binds an echinenone (ECN) carotenoid and mediates photoprotection in cyanobacteria. In the dark, OCP assumes an orange, inactive state known as OCP^O; blue light illumination results in the red active state, known as OCP^R. The OCP^R state is characterized by large-scale structural changes that involve dissociation and separation of C-terminal and N-terminal domains accompanied by carotenoid translocation into the N-terminal domain. The mechanistic and dynamic-structural relations between photon absorption and formation of the OCP^R state have remained largely unknown. Here, we employ a combination of time-resolved UV−visible and (polarized) mid-infrared spectroscopy to assess the electronic and structural dynamics of the carotenoid and the protein secondary structure,

from femtoseconds to 0.5 ms. We identify a hereto unidentified carotenoid excited state in OCP, the so-called S* state, which we propose to play a key role in breaking conserved hydrogen-bond interactions between carotenoid and aromatic amino acids in the binding pocket. We arrive at a comprehensive reaction model where the hydrogen-bond rupture with conserved aromatic side chains at the carotenoid β1-ring in picoseconds occurs at a low yield of <1%, whereby the β1-ring retains a *trans* configuration with respect to the conjugated π-electron chain. This event initiates structural changes at the N-terminal domain in 1 μs, which allow the carotenoid to translocate into the N-terminal domain in 10 μs. We identified infrared signatures of helical elements that dock on the C-terminal domain β-sheet in the dark and unfold in the light to allow domain separation. These helical elements do not move within the experimental range of 0.5 ms, indicating that domain separation occurs on longer time scales, lagging carotenoid translocation by at least 2 decades of time.
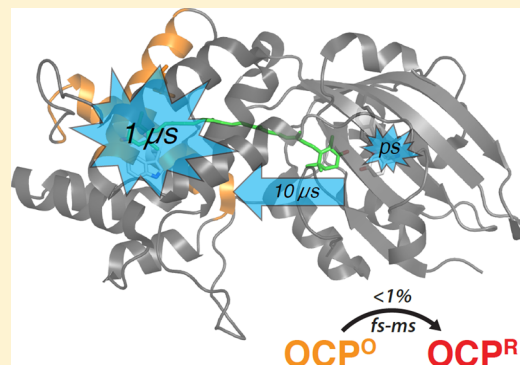
INTRODUCTION

Photosynthetic organisms contain an elaborate photoprotection apparatus to regulate oxidative stress under varying light conditions.[1−3] Carotenoids are essential agents that carry out nonphotochemical quenching (NPQ), as has been well-established in plants and algae within the thylakoid membrane.[2,4,5] In cyanobacteria, however, the primary quenching process follows a different mechanism facilitated by a small water-soluble carotenoid-containing protein known as the orange carotenoid protein (OCP).[3,6,7] Several studies have identified the complex photoactive behavior of OCP involving conversion from an orange form (OCP^O) to a red form (OCP^R),[8] encompassing a series of reversible structural changes of carotenoid and secondary/tertiary structure,[9−15] culminating with energy dissipation in the phycobilisome (PBS) antenna complex.[7,16,17] However, many of the dynamic

aspects of this mechanism remain largely unexplored and are technically challenging given the very low quantum yield of the OCP photochemical processes.[8]

OCP contains two principal structural elements: an all α-helical N-terminal domain and a mixed α/β C-terminal domain.[18,19] The C-terminal domain is considered the primary regulator of the photosensory response of OCP, while the N-terminal domain is viewed as a downstream effector later involved in phycobilisome binding. These domains encapsulate a single noncovalently bound keto-carotenoid [3′-hydroxyechinenone (ECN)] lying in a crevice oriented lengthwise across the protein and insulated from the solvent. Hydrogen bonds between the terminal ECN β1-ring carbonyl group and

nearby W288 and Y201 residues are illustrated in Figure 1. The opposite β2-ring is slotted between aromatic residues

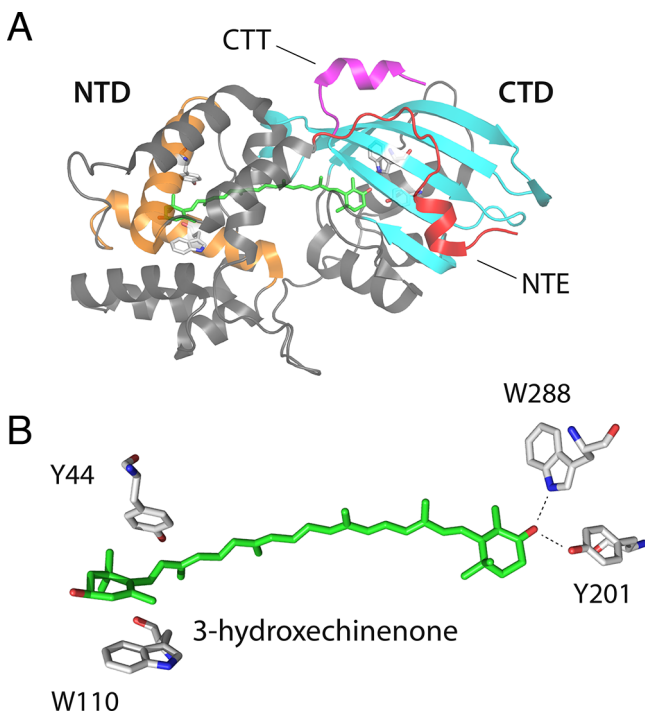**Figure 1.** (A) OCP dark state structure (OCP^O) derived from X-ray crystallography (PDB: 5UI2) with mediating β-sheet (blue) and relevant terminal helical domains, NTE (red) and CTT (magenta), highlighted. (B) 3′-Hydroxyechinenone chromophore (ECN) and neighboring residues implicated in the light-induced response of OCP.

W110 and Y44 within the N-terminal domain, resulting in a strained and bent conformation. The entire cofactor is packed against several hydrophobic residues along the polyene chain.

Upon photoactivation with a blue flash, a red form of OCP is formed within picoseconds at a very low yield on the order of percents,[8] indicating that interactions between the ECN and the protein have been changed on that time scale. Ultimately, this photoactivation event results in dissociation of the N-terminal and C-terminal domains[11−13] and carotenoid translocation by 12 Å into the N-terminal domain,[11] allowing for phycobilisome binding[20] and facilitating the ultimate OCP photoprotective function.[3] These known features imply that during the photoreactions, rupture of the ECN β1-ring−Y201/W288 hydrogen-bonding interaction occurs to release the carotenoid into the N-terminal domain and that the N-terminal extension (NTE, also known as αA helix), which docks on the C-terminal β-sheet through a long loop (Figure 1A, red), must dissociate from the β-sheet face to allow domain separation. Additionally, a short helix on the C-terminus, the C-terminal tail (CTT), was recently identified as a potentially important control element that docks on the C-terminal domain β-sheet in the OCP^O state (Figure 1A, magenta) but may switch position to cover the empty carotenoid tunnel of the C-terminal domain in the OCP^R state.[21] Yet, the mechanistic and dynamic-structural relations between photon absorption and formation of the OCP^R state remain largely unclear. The photochemical event that breaks the interactions between ECN and the aromatic side chain in the C-terminal domain is essentially unknown, as are the

events and their timing that mechanistically couple the photochemistry with structural dynamics in the protein, carotenoid translocation and domain separation.

In this report, we utilize various UV−vis and infrared spectroscopies in tandem to characterize the photoactivation mechanism of OCP. First, transient UV−vis absorption spectroscopy (UV−vis TA) was employed to probe the evolution of the ECN electronic state, from femtoseconds to 500 μs, as the photocycle unfolded. This provided an approximate idea of the number of intermediate steps spanning ultrafast excited-state energy dissipation upon photon absorption to spectral evolution induced by protein structural changes greater than 8 decades later in time. To gain further molecular insight in these transformations, we next turn to vibrational spectroscopy. Polarized ultrafast infrared spectroscopy was used to evaluate the isomeric state of the ECN β1-ring, which provides key information for the primary photoactivation mechanism. Then, we use difference FTIR spectroscopy on wild-type and mutant OCP to assess the IR signature of specific secondary structure elements. Finally, with infrared transient absorption spectroscopy (mid-IR TA), we determine the structural dynamics from the picosecond leading up to the millisecond time scale that underlies OCP photoactivation. We find that, contrary to previously suggested reaction models, no isomerization of the ECN β1-ring occurs on photoactivation. We also observe that significant structural changes in the N-terminal domain occur in approximately 1 μs, prior to the motion of the CTT and NTE helices, which occurs on time scales longer than 1 ms and are prerequisite for domain separation. Our results indicate that, most likely, carotenoid translocation occurs on a 10 μs time scale and thereby precedes domain separation by at least 2 decades of time.

■ RESULTS AND DISCUSSION

ECN Dynamics in OCP: Femtosecond to Submillisecond UV−Vis TA Spectroscopy Reveals Carotenoid Dynamics. Ultrafast electronic and vibrational spectroscopies are powerful tools to assess reaction mechanisms in photoreceptor proteins, especially now that synchronized Ti:sapphire laser systems allow expansion of such measurements to the millisecond time scale in a single experiment.[22−30] Here, we recorded transient femtosecond to submillisecond UV−vis and mid-IR TA spectra to probe the OCP electronic and vibrational states during its photoactivation reaction. In this study, recombinant ECN-containing *Synechocystis* OCP was employed. We first discuss the electronic spectral evolution that reports on the photocycle dynamics from the perspective of the ECN chromophore. Kinetic parameters were estimated through global analysis using the Glotaran software package and are reported as evolution-associated difference spectra (EADS), where the individual components evolve into the next assuming a sequential reaction scheme with increasing lifetimes.[31,32] OCP was excited at 475 nm.

The femto- to picosecond dynamics of OCP was characterized before[8,33,34] and involves excitation of the optically allowed S$_2$ state and ultrafast internal conversion in ≈100 fs to the optically dark S$_1$ state, which is coupled to an intramolecular charge-transfer (ICT) state. The S$_1$/ICT state decays to the ground state on the picosecond time scale. We obtained a similar result [Figure S1, Supporting Information (SI)], with the exception that in addition to the 1.4 and 4.5 ps S$_1$/ICT lifetimes, a previously unobserved slowly decaying

fraction of excited states was detected with a lifetime of 24 ps at an amplitude of ≈5% of the initially formed S_1/ICT state. Its spectral signature shows an overall blue-shift and sharpening with respect to the S_1/ICT state, which leads us to conclude that it corresponds to a small population of a purported S* state,[35] which has been observed and characterized for open-chain carotenoids in photosynthetic light-harvesting complexes,[36−40] keto-carotenoids in plant light-harvesting complexes,[41] carotenoids with long conjugation lengths in solution,[36,42−44] and artificial light-harvesting constructs.[45,46] The full set of time-gated spectra and fits is given in Figure S2 (SI). Here, the spectral signature of the S* state is clearly visible in the raw spectra at time delays between 15 and 50 ps. The initially populated, short-lived S_2 state was not resolved in our experiments due to sparse temporal sampling around time zero.

After S_1/ICT and S* state decay, a primary photoproduct that is red-shifted with respect to the OCP^O state is observed at very low amplitude. This is evident in the EADS of the photoproducts, shown in Figure 2A. Figure S1B (SI) shows the
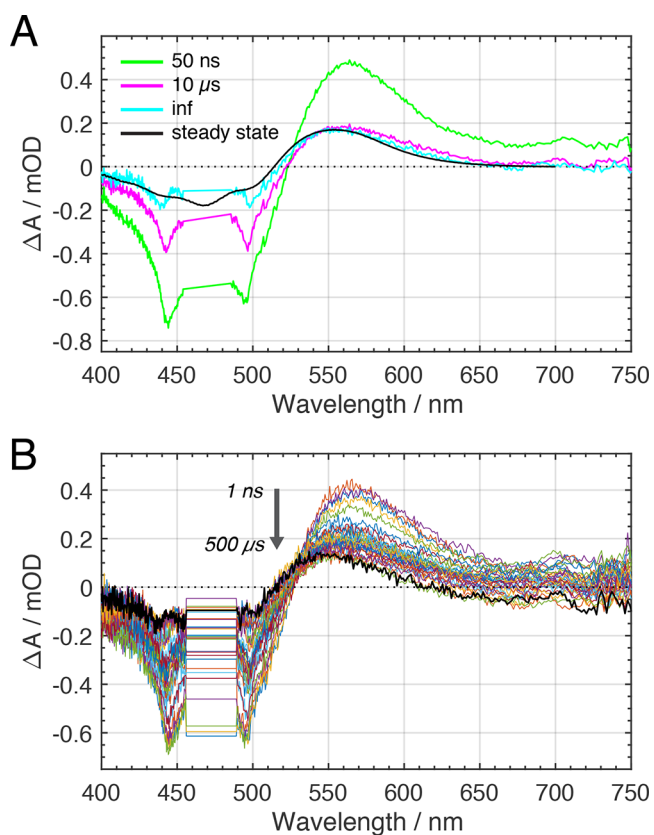

Figure 2. (A) Slowest EADS derived from global analysis of UV−vis TA data of OCP are overlaid with the difference (light minus dark) UV−vis absorption spectrum. (B) Raw time-gated UV−vis TA spectra from 1 ns to 500 μs. Note that the data between 454 and 485 nm have been omitted due to scatter from the excitation pulse.

normalized EADS. The primary photoproduct (green) shows an absorption maximum at 563 nm and a zero-crossing at 523 nm, at an amplitude that corresponds to approximately 0.5% of the initially populated excited states (cf. Figure S1A,C, SI), somewhat lower than observed for native *Synechocystis* OCP.[8] Given that the ground state bleach of the OCP^O state and induced absorption of the product partially compensate each

other,[8] a quantum yield for the primary photoproduct of 1.5% may be estimated (Figure S3, SI). It was noted previously that this primary photoproduct corresponds to a red form of ECN but is red-shifted by ≈12 nm with respect to the steady-state OCP^R state.[8] This observation implies that the primary photoproduct, where ECN presumably resides near its original binding pocket halfway between the C-terminal and N-terminal domains, has an absorption spectrum that is different from that of the OCP^R form, where ECN has translocated into the N-terminal domain.[11] Given that the precise ECN absorption spectrum results from its conformation and interactions with the protein in its binding pocket, the dynamics of the photoproduct likely reports on the ECN motion toward and into the N-terminal domain, as described below.

Figure 2B displays raw time-gated spectra at delays between 1 ns and 500 μs. The amplitude of the product significantly decreases as time progresses, whereas the overall spectrum shifts to the blue, indicating that (i) the population of photoproducts decreases and (ii) the ECN conformation and environment change as a function of time and start to resemble the OCP^R state. The evolution described above is well-represented by the global analysis of the photoproduct dynamics shown in Figure 2A. The primary photoproduct (green), denoted P_1 here, has an absorption maximum at 563 nm and a zero crossing at 523 nm, and is formed at a quantum yield of 1.5%. It evolves to the magenta EADS in 50 ns, which involves a drop in amplitude by ≈60% and a blue-shift of the absorption maximum by 7 nm to 556 nm and of the zero-crossing by 1 nm to 522 nm. We denote this secondary photoproduct as P_2, which is formed at a net yield of 0.40 × 1.5% = 0.6%. Subsequently, P_2 (magenta line) evolves to the final EADS (cyan line) in 10 μs, involving a further blue-shift of the absorption maximum by 4 nm to 552 nm and of the zero crossing by 4 nm to 518 nm. This final EADS does not evolve on the time scale of the experiment and is denoted as P_3. The steady-state light-minus-dark spectrum, representing the OCP^R minus OCP^O spectrum, is shown as the black line. It has its maximum absorption at 552 nm, identical to that of P_3, and a zero crossing at 515 nm, 3 nm blue-shifted with respect to P_3.

We interpret these dynamics in the following way: There is general consensus that OCP^R represents a state where the hydrogen bonds between the ECN β_1-ring and W288/Y201 are broken, the carotenoid has planarized, and ECN translocates by 12 Å into the N-terminal domain.[8,11,47,48] P_1 (Figure 2A, green line) represents the primary photoproduct that is formed after decay of the ECN S_1/ICT excited state, has an absorption that is red-shifted by 11 nm with respect to OCP^R, and shows no vibronic structure. Given the overall similarity between P_1 and OCP^R, we propose that P_1 represents a state where, as in OCP^R, the hydrogen bonds between the ECN β_1-ring and W288/Y201 are broken and its configuration is planar, but ECN is still located in or close to its original binding site between the N-terminal domain and C-terminal domain. P_1 (green line) evolves to P_2 (magenta line) in 50 ns. The amplitude loss involved in this evolution indicates that a fraction of P_1 products reverts to OCP^O in 50 ns by re-forming hydrogen bonds with W288 and Y201 due to the close resemblance to its native state. Concomitantly, the photoreaction proceeds as a reactive fraction of ≈40% of ECN in the P_1 state moves away from its original position and forms P_2. P_2 has a blue-shifted absorption with respect to P_1, indicating altered interactions with its protein environment, supporting

the interpretation that ECN is located in a different position. P_2 evolves to the next product P_3 (cyan line) in 10 μs. This evolution involves a further blue-shift, while retaining product amplitude. P_3 does not further evolve on the time scale of the experiment of 750 μs. For comparison, Figure 2A shows the OCP^R minus OCP^O steady-state difference spectrum (black line). We observe that P_3 is similar to the steady-state difference spectrum, with identical absorption maximum and only a 3 nm red-shift of the zero crossing. Hence, P_3 and OCP^R may be very similar with regard to direct pigment−protein interactions, with the remaining differences in interaction between ECN and its environment occurring on time scales >1 ms.

The data described above were taken at relatively high excitation power and initial signal amplitude, which were necessary conditions to track the dynamics of the low-yield P_1−P_3 photoproducts. In Figure S4 (SI) we present an experiment with ∼2.5 times lower excitation energy. This experiment was performed with a stretched excitation pulse of ∼2 ps duration, which means that the peak excitation power was 20 times lower than with a femtosecond excitation pulse of the same energy. Through these combined effects, the peak power density on the sample was ∼50 times lower than the results presented in Figures 2 and S1 and S2 (SI). We observe a spectral evolution that is very similar to that at high excitation power, with similar time constants and EADS, well-resolving the S* state and the P_1 state. The spectra of P_2 and P_3 are consistent with those presented for high energy excitation, albeit poorly resolved because at these low signal amplitudes, noise and baseline fluctuations become limiting in the detection. Thus, this experiment demonstrates that the key features described for Figures 2 and S1 and S2 (SI) are genuine and do not relate to the high excitation energy used.

We have shown above, for the first time to our knowledge, the spectrally resolved photoproduct dynamics in the UV−vis of OCP from the femtosecond to (sub)millisecond time scale. Recently, Maksimov et al. reported a single-wavelength flash photolysis study of OCP with a time resolution of 200 ns.[15] They found a major decay phase of the photoproduct at 550 nm by 30% with a time constant of 300 μs at 36 °C, which slowed down to the millisecond time scale on lowering the temperature to 20 °C.

Orientation of the ECN Carotenoid β_1 Ring in OCP^O and OCP^R. One important question regarding OCP photoactivation concerns the mechanism of hydrogen bond rupture between the ECN β_1-ring and the W288 and Y201 side chains in the C-terminal domain, which is a prerequisite for ECN translocation into the N-terminal domain in the OCP^R state. One proposed mechanism concerns photoinduced s-isomerization of the ECN C6−C7 single bond, which would flip the orientation of the β_1-ring by 90° going from an s-trans to an s-cis conformation. Such photoinduced isomerization mechanisms that rupture or rearrange hydrogen-bonding networks are commonly in effect in photoreceptor proteins such as microbial rhodopsins, photoactive yellow protein, and phytochromes.[49−53] Support for such a mechanism in OCP came from the X-ray structure of the isolated N-terminal domain (also known as red carotenoid protein, RCP) containing a different keto-carotenoid, canthaxanthin, exhibiting a C6−C7 s-cis conformation[11] and from resonant Raman spectroscopy, where such a conformation would be one of the structures consistent with (but not exclusively) the OCP^R Raman spectra.[47] Raman optical activity (ROA) experiments

compared ROA with structure-based calculations and found that OCP^O and OCP^R ROA spectra were consistent with OCP^O and RCP X-ray structures.[48] However, they did not test whether an s-trans C6−C7 conformation would reproduce their ROA spectra for OCP^R. On the other hand, a time-resolved X-ray crystallographic structure study did not reveal any change in the isomeric C6−C7 composition of OCP after photoactivation.[54]

To assess the orientation of the ECN β_1-ring in the OCP^O and OCP^R states, we performed a visible pump/mid-IR probe absorption anisotropy experiment. A similar approach was used to track tetrapyrrole ring motion in phytochromes.[55] Figure 3
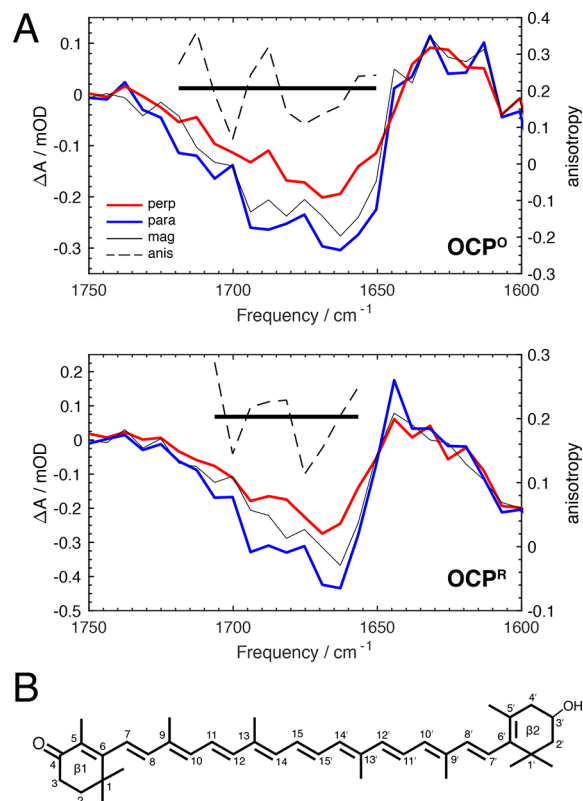

Figure 3. (A) Mid-IR anisotropy spectra with optical excitation at 475 nm and mid-infrared probing taken at a 2 ps time delay, with parallel polarization in blue, perpendicular polarization in red, and magic angle in thin black (left vertical axis), for OCP^O (upper panel) and OCP^R (lower panel). The anisotropy (right vertical axis) is plotted with the dashed line, with the average indicated with the thick solid black line. (B) 3′-Hydroxyechinenone chemical structure with C6−C7 in a trans conformation, with atomic numbering included.

shows anisotropy spectra for OCP^O and OCP^R with optical excitation of ECN at 475 nm. The spectra were taken at a time delay of 2 ps, which implies that photoexcited ECN resided in the S_1/ICT excited state. We observe a ground-state bleach of the ECN β_1-ring C=O group around 1680 cm^{-1} and a photoinduced absorption around 1630 cm^{-1} (Figure 3A, upper panel), indicating that the ECN C=O downshifts its frequency as a result of optical excitation, a commonly observed phenomenon that results from decreased bond order during π−π transitions.[56] The angle (Θ) between electronic and vibrational transition dipoles was determined using the anisotropy $r = (\Delta A_\parallel - \Delta A_\perp)/(\Delta A_\parallel + 2\Delta A_\perp)$, where $\Delta A_\parallel$ is the mid-IR ΔA signal with parallel polarization with respect to the visible pump beam and $\Delta A_\perp$ the mid-IR ΔA

signal with perpendicular polarization with respect to the visible pump beam, and the expression $r = 2/5[(3 \cos^2 \Theta - 1)/2]$.[57] We assumed that the electronic transition dipole moment is polarized along the polyene backbone. We found an anisotropy value $r = 0.23$ for OCP^O (Figure 3A, upper panel), corresponding to $\Theta \approx 30°$, indicating that the ECN β1-ring assumes a *trans* conformation in the OCP^O state (Figure 3B), consistent with the X-ray structures of OCP^O.[18,19] Strikingly, in the OCP^R state we observe an essentially identical anisotropy $r = 0.20$ (Figure 3A, lower panel), which implies that Θ remains identical in the OCP^R state. A C6−C7 s-*cis* conformation would result in an approximately 90° angle between the transition dipole moments of the β1-ring carbonyl mode and the ECN polyene backbone, which would correspond to $r = -0.2$, which is not observed experimentally. Hence, we conclude that ECN retains a β1-ring *trans* conformation and that the C6−C7 single bond does not isomerize upon photoactivation. This finding contrasts with the β1-ring conformation resolved in the X-ray structure of the isolated N-terminal domain[11] but agrees with a recent time-resolved X-ray study that revealed no large motions of the β1-ring upon photoactivation.[54] Our finding is also consistent with results from ultrafast spectroscopy on the OCP^R state, which indicate an increased ICT character of the S$_1$ state.[58] For such a phenomenon to occur, the β1-ring carbonyl needs to be in conjugation with the polyene backbone, which is maximized in a *trans* conformation and minimized in *cis*.[59] We may conclude that with regard to the β1-ring orientation, the isolated canthaxantin-binding N-terminal domain is not a good model for ECN-OCP^R given the existence of protein−side chain interactions induced by the β1-carbonyl. This influence is evident with the varying kinetics of photoactivation, recovery, and PBS fluorescence quenching.[60] A resonant Raman study showed that the OCP^O to OCP^R transition involves either a C6−C7 isomerization or a diminished bending of the ECN rings with respect to the conjugated polyene backbone plane.[47] Our present study rules out the former possibility.

Having established that the anisotropy spectra indicate an absence of isomerization of the ECN chromophore in the conversion from the OCP^O to OCP^R form (Figure 3), this observation begs the question of what initiates hydrogen bond disruption near the chromophore. Yang and co-workers hypothesized a ECN tautomerization following photon absorption.[54] In this model, electronic excitation induces a shift in the keto−enol equilibrium of the β1-ring. Subsequent bond order changes would lead to rupture of the hydrogen bonds with Y201 and W288 releasing strain stored in the native bent chromophore, followed by rapid reversion of the high-energy enol form. However, we note that the involved methyl group of the β1-ring is not acidic at all, which renders the enol form a particularly high-energy species unlikely to be involved in the OCP photoreaction.

The conserved hydrogen bonds with Y201 and W288 are not expected to rupture while the ECN chromophore resides in the S$_1$/ICT state, as this state is not known to be associated with significant geometrical distortions. On the other hand, the observation of the S* state in the excited-state dynamics may be significant for the OCP reaction mechanism. It has been proposed that S* represents a structurally distorted form of the optically forbidden S$_1$ state.[35,42,44] For OCP-bound ECN, transient population of the S* state would lead to significant structural strain on the polyene backbone that may be sufficient to break the hydrogen bonding to the β1-ring in a

small number of cases corresponding to the ≈1.5% primary quantum yield. After hydrogen bond rupture, the strain in ECN that is present in the OCP^O ground state (as evidenced by the bent and twisted conformation resolved in the X-ray structure) may be released and ECN may assume a planar, relaxed conformation that brings the β1-ring C═O out of hydrogen bonding distance with W288 and Y201, resulting in a metastable red-shifted ECN species from which the OCP photoreaction further proceeds.

Identification of Mobile Helical Segments by FTIR Spectroscopy. In the section further below the picosecond to submillisecond mid-IR dynamics of OCP will be presented to pinpoint changes in its secondary structure. For proper interpretation, we first identify mobile secondary structure segments by means of FTIR spectroscopy of wild-type and mutant OCP. Figure 4 shows the light-minus-dark FTIR

Figure 4. Light-minus-dark difference FTIR spectra of wild-type OCP (black), the δNTE mutant (magenta), and the δCTT mutant (cyan) in H$_2$O and D$_2$O buffers.

spectra of wild-type OCP in H$_2$O buffer (black), along with that of a mutant where the NTE has been deleted (magenta, hereafter referred to as the NTE mutant) and a mutant where CTT has been deleted (cyan, hereafter referred to as the CTT mutant). The wild type spectrum is similar to those reported earlier[8,9] and is dominated by a large negative signal in the Amide I region with bands at 1653, 1644, and 1625 cm^{-1}, flanked by positive signals at 1665 and 1620 cm^{-1}. The bands at 1653 (−), 1644 cm^{-1} (−) and 1665 (+) cm^{-1} may be assigned to structural changes in helical elements, while those at 1625 (−) and 1620 (+) cm^{-1} are likely due to changes in the β-sheet. In the NTE mutant (ΔNTE, magenta line), the band at 1644 cm^{-1} almost completely disappears, while that at 1653 cm^{-1} remains intact. Likewise, in the CTT mutant (ΔCTT, cyan line), the 1644 cm^{-1} band disappears entirely.

Figure 4 also shows the corresponding difference FTIR spectra in D_2O buffer. It is important to measure these for comparison with the time-resolved IR experiments reported below, which were conducted in D_2O buffer to avoid the strong water absorption in the Amide I region. In wild-type OCP (black), the overall pattern is similar to that in H_2O, but with a downshift of the 1644 cm^{-1} band to 1638 cm^{-1}, a decrease in amplitude of the 1653 cm^{-1} band, and an increase of the positive band at 1620 cm^{-1}. The ΔNTE mutant (magenta) shows a large loss of the 1638 cm^{-1} band, but with some remaining amplitude, while the 1653 cm^{-1} band remains intact. As in H_2O, the ΔCTT mutant signal (cyan) is similar to that of the ΔNTE mutant.

We interpret these results as follows: (i) In H_2O, both the NTE and CTT helices have their IR band at 1643 cm^{-1}. (ii) In D_2O, both the NTE and CTT helices have their IR band at 1638 cm^{-1}. (iii) The NTE and CTT helices must respond in concert; i.e., unfolding of one requires movement and/or unfolding of the other. Otherwise, in H_2O buffer, there would be a significant signal left at 1643 cm^{-1} in either mutant, which is not the case. A similar case was observed in the LOV2 domain of plant phototropin, where a short N-terminal helix and a long C-terminal helix docked on the same β-sheet were found to unfold in concert.[28,61] (iv) There is another helical element that absorbs at 1655 cm^{-1} in H_2O and shifts to $\approx$1640 cm^{-1} in D_2O. This is supported by the higher amplitude of this band in H_2O as compared to D_2O and represents the residual signal at 1640 cm^{-1} in the mutants.

With this information at hand, we now proceed to the picosecond−millisecond mid-IR TA spectroscopy to assess the secondary structure dynamics in OCP upon photoactivation.

Picosecond to Millisecond Dynamics of OCP: Time-Resolved Mid-IR Spectroscopy Reveals Protein Motions in the N-Terminal Domain. Transient mid-IR data taken on OCP upon excitation at 475 nm are presented in Figure 5, along with results of global fitting. A stretched picosecond pulse was used for excitation in order to maximize photoproduct formation through more efficient singlet excitation.[28] In the case of OCP, the photoproduct was further enhanced because the ECN excited state largely decays in 2.5 ps, which enables multiple rounds of excitation during the picosecond pulse. Kinetic parameters were estimated through global analysis using the Glotaran software package and are reported as EADS assuming a sequential reaction scheme with increasing lifetimes as with the UV−vis data above.[31,32] Individual traces at notable frequencies along with the result of the global fit are provided in Figure 5B. The full set of kinetic traces is given in Figure S5 (SI), and the transient concentration of the various states is given in Figure S6 (SI).

The first component, with a 3 ps lifetime (Figure 5A, black), has a lifetime very similar to that of the ECN S_1/ICT state shown above. It exhibits a strong broad negative signal at 1685 cm^{-1} that is assigned to the bleach of the ECN β1-ring C=O stretch mode upon population of the optically forbidden S_1/ICT state of ECN, which immediately follows excitation of the allowed S_2 state in 100 fs.[8] The peak frequency of the ECN C=O band is significantly red-shifted from ECN in solution (1730 cm^{-1}, Figure S7, SI), supporting the prediction of strong hydrogen bonding to the nearby side chains of W288 and Y201, as observed in crystal structures (Figure 1B).[18,19] Upon decay of ECN S_1/ICT in 3 ps, a species is observed that has a lifetime of 23 ps (red line). Its spectrum is characterized by a smaller bleach in the carbonyl stretch region and a red-shifted
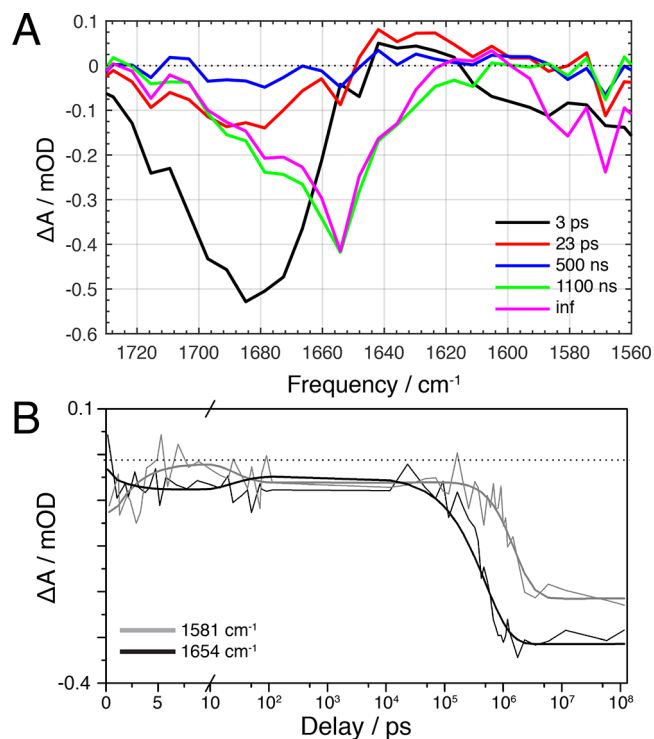

Figure 5. (A) EADS determined from global analysis of mid-IR transient absorption data. (B) Kinetic traces at 1581 (gray) and 1654 cm^{-1} (black), with fitting results overlaid. The 1581 cm^{-1} trace was expanded by a factor 2.5 to facilitate comparison with the 1654 cm^{-1} trace.

induced absorption band at 1635 cm^{-1}. Its lifetime is similar to the 24 ps lifetime of the UV−vis experiment, albeit at a higher amplitude of about 15% of the initial signal, which indicates that this component likely represents a fraction of slowly decaying ECN S* species. The next EADS (blue line) is formed in 23 ps and has an overall low amplitude. It exhibits a small bleach near 1680 cm^{-1} that barely rises above the noise. This small bleach coincides with the ECN C=O and, hence, reports on a long-lived structural change of the carotenoid, consistent with the primary photoproduct P_1 being formed at low yield. Given the limited signal-to-noise in this experiment, its relative amplitude is difficult to estimate but appears somewhat higher than expected from the ∼1.5% quantum yield estimated from the UV−vis experiment above, commensurate with the use of a stretched picosecond excitation pulse, which allows multiple rounds of excitation within the pulse duration.

The ensuing spectral evolution on time scales longer than 1 ns is peculiar and requires two closely spaced time constants of 0.5 and 1.1 μs. First, the low-amplitude blue EADS evolves into the green EADS in 0.5 μs. We observe growth of a broad and strong bleach centered around 1655 cm^{-1}, with shoulders near 1680 and 1635 cm^{-1}, and nearly zero amplitude elsewhere. Figure 5B shows the kinetic trace at 1654 cm^{-1}, which demonstrates a clear rise of the signal from almost zero initial amplitude. Then, in 1.1 μs, an additional bleach near 1570− 1580 cm^{-1} rises. The rise of the 1654 and 1581 cm^{-1} signals are discongruous, as demonstrated in Figure 5B: the 1581 cm^{-1} rise (gray line) is clearly delayed with respect to that at 1654 cm^{-1} (black line), rationalizing the need for two closely spaced time constants in the global analysis. The relative amplitudes of the green and magenta EADS are difficult to estimate as a result of the low transient concentration of the

former (Figure S6A, SI). Importantly, no further spectral evolution is observed out to the experimental time window of 120 μs. Figure S8 (SI) shows raw spectra up to 585 μs from another data set that indicate that no further spectral evolution occurs up to that time.

The green EADS clearly represents the rise of an Amide I signal in 0.5 μs, as ECN has no IR-active vibrational modes in this spectral region. Its maximum near 1655 cm^{-1} implies that it mainly represents loss of α-helix, with possible minor contributions from β-sheet (shoulder near 1630 cm^{-1}) and turn/loop structural changes (shoulder near 1680 cm^{-1}). The magenta EADS, which evolves from the green EADS in 1.1 μs, has a similar signal in the amide I region but shows an additional bleach around 1570 cm^{-1}. The latter signal may be assigned to amide II modes in the protein backbone.

Before proceeding with the interpretation of the EADS, we first need to rationalize the discongruous rise of Amide I and II bands. Upon dissolving a protein in D$_2$O buffer, solvent-exposed parts of the secondary structure will undergo H/D exchange, readily exchanging the protons at the backbone amides to deuterons. In such a case, the Amide II band will downshift by >100 cm^{-1} to 1450 cm^{-1}.[62] In contrast, buried parts of the secondary structure will exchange much slower or not at all, and the backbone amides will largely retain their protons, resulting in an Amide II band near 1570 cm^{-1}. Intermediate cases are also possible if H/D exchange is slower than the time elapsed between immersion in D$_2$O and the experiment (*in casu* 18 h at 4 °C), which may result in relatively buried elements being (partly) exchanged. In our time-resolved experiments, the green EADS, which rises in 0.5 μs, lacks an Amide II band and may therefore be regarded as a fully H/D exchanged secondary structure element. The magenta EADS, which evolves from the green EADS in 1.1 μs, does exhibit an Amide II band near 1570 cm^{-1} and therefore represents, at least in part, a nonexchanged secondary structure element. It is not clear if the observed exchanged−nonexchanged dynamics in 0.5 and 1.1 μs is sequential, with a nonexchanged element following an exchanged element, or if it is heterogeneous, where a mixture of exchanged and nonexchanged helical elements in the ensemble of OCP proteins exhibit slightly different reaction rates. Figure S6B−D (SI) shows an analysis in terms of a parallel evolution from the initially formed ECN photoproduct. Given the limited signal-to-noise of the data, we will not further interpret this kinetic difference, and we regard it as essentially a single set of structural changes on the 0.5−1.1 μs time scale.

We now discuss the origin of the rising Amide I signal at 1655 cm^{-1}. Figure 6 shows an overlay of the nondecaying EADS with the light-minus-dark FTIR spectrum of OCP in D$_2$O. Clearly, the 1655 cm^{-1} band overlaps with the 1653 cm^{-1} band in the FTIR spectrum but not with the large negative band at 1638 cm^{-1}. Thus, bearing the FTIR experiments of Figure 4 in mind, these experiments clearly demonstrate that the helical element that causes the 1655 cm^{-1} signal and rises on the submicrosecond time scale does not correspond to the NTE helix nor to the CTT helix. HDX−MS experiments showed that the C-terminal domain secondary structure remains largely intact in the OCP^R state.[12] Hence, we conclude that the 1655 cm^{-1} signal most likely originates from the all-helical N-terminal domain. Strikingly, the nondecaying, magenta EADS has a final amplitude that is significantly larger than that of the blue EADS (Figure 5A), although their relative amplitudes are difficult to estimate because of the already
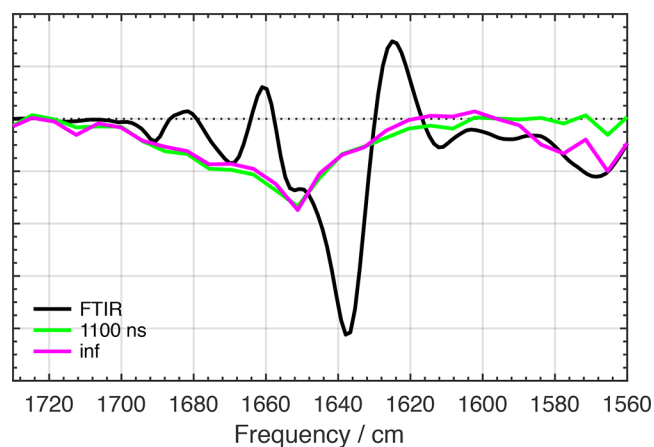

Figure 6. Light-minus-dark difference FTIR spectrum for wild-type OCP in D$_2$O buffer (black line) with 1.1 μs EADS (green line) and nondecaying EADS (magenta line) overlaid.

noted uncertainty of the latter. Because the blue EADS corresponds to the bleach of a single ECN C=O band, the nondecaying EADS must involve a multitude of Amide I oscillators. We refer to this particular state rising on the 0.5−1.1 μs−time scale as P$_2'$.

Importantly, up to 585 μs, the time limit of our time-resolved IR experiment, there is no indication of a rise of the large negative 1638 cm^{-1} band that was assigned to the NTE and CTT helices. Given that such motions are a prerequisite for domain separation, we infer that domain separation occurs at time scales >0.5 ms. We conclude that structural changes in the N-terminal domain precede motion of the NTE and CTT helices and domain separation by at least 3 decades of time.

The OCP Reaction Mechanism. The results described above from static FTIR and time-resolved electronic and vibrational spectroscopy allow us to paint a picture of OCP photoactivation, from photon absorption to carotenoid translocation and domain separation, notated in Figure 7. Upon excitation, the ECN relaxes to the optically forbidden S$_1$/ICT excited state in 100 fs, with a minority population of the S* excited state. Noting that the S* excited state may represent a structurally distorted form of the S$_1$ state,[42,44] we speculate that population of the S* state strains the hydrogen bonds with W288 and Y201, resulting in their rupture at a low yield of $\approx$1.5%. The S$_1$/ICT and S* states then relax to the electronic ground state in picoseconds, resulting in the primary ground-state photoproduct P$_1$, a structurally relaxed, planar ECN that has its electronic absorption red-shifted and retains a C6−C7 *trans* configuration. We argued above that light-driven C6−C7 *trans*−*cis* isomerization[11,47] or β1-ring keto−enol equilibrium shifts[54] are unlikely to constitute the primary photochemical event in OCP.

With the strongest interaction of ECN with the C-terminal domain gone (i.e., hydrogen bonds to W288 and Y201) and its conformational strain released, ECN finds a new quasi-equilibrium position in the OCP binding pocket, leading to the P$_2$ product in 50 ns (cf. Figure 2). About 60% of the P$_1$ product states re-form the hydrogen bonds with W288 and Y201 to regenerate the original OCP^O state with this time constant.

On the 0.5−1.1 μs time scale, helical elements in the N-terminal domain undergo structural changes or change position, resulting in the P$_2'$ state (cf. Figure 5). In the N-
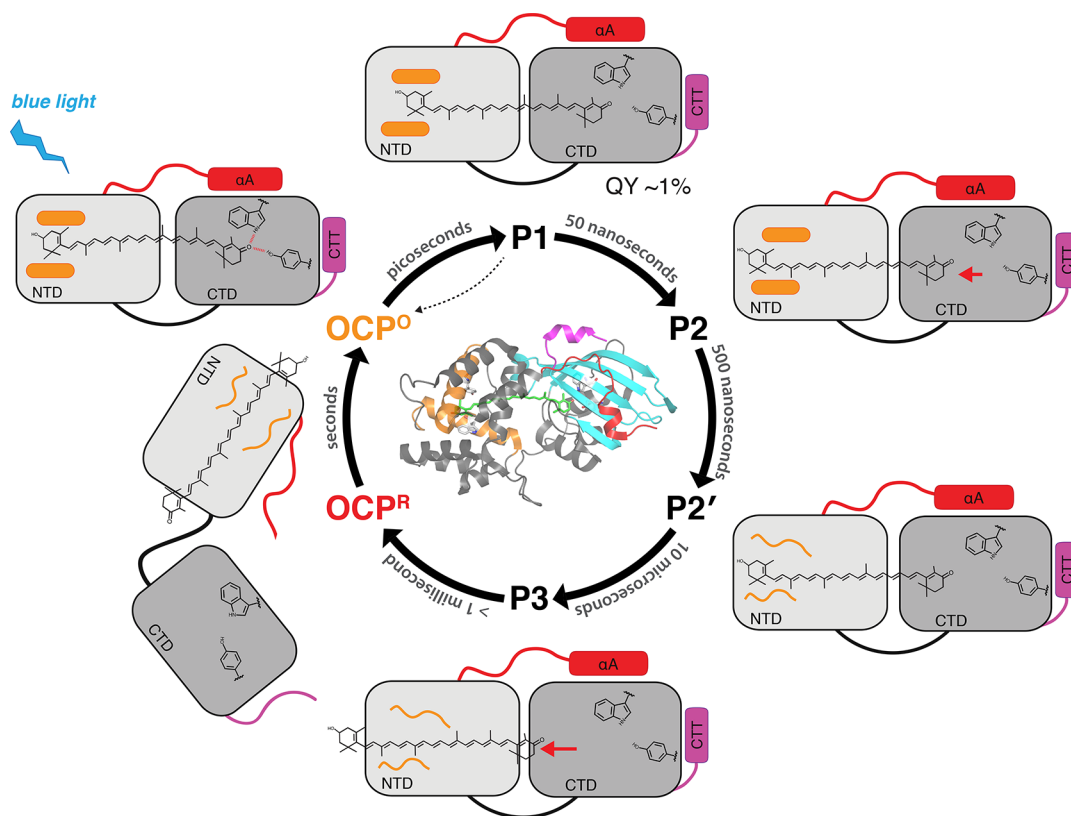
Figure 7. Model of OCP photoactivation mechanism derived from various UV−vis and mid-IR spectroscopic experiments.

terminal domain, significant helical changes are expected to occur upon photoactivation that mainly relate to the 12 Å translocation of the ECN.[11] Comparing the OCP^O structure[18,19] with the isolated N-terminal domain structure,[11] it is observed that in isolated N-terminal domain, E34 moves and performs a rotation with respect to the OCP^O structure,[11] as shown in Figure 8A. Notably, this residue is located on helix C, which tilts by 6° when comparing the N-terminal domain to OCP^O. In addition, there is a constriction in the carotenoid tunnel in OCP^O formed by L37, M83, and M117 (Figure 8B, blue), which are located on helices C, E, and G, respectively. Finally, the $\pi-\pi$ stacking interactions between the ECN β_2-ring and Y44/W101 must be disrupted in the OCP^R state (Figure 8B). For the carotenoid to translocate and pass the bottlenecks described above, the α-helices carrying these amino acids must rotate and move aside, and they are likely the origin of the rise of the P$_2'$ Amide I signals and the Amide I signal at 1655 cm^{-1} in the FTIR spectrum. (Figures 4-6).

The questions arise: what triggers the structural changes in the N-terminal domain on this (sub)microsecond time scale, and what is their significance for the photoreaction? The dynamics of N-terminal domain helical changes represented by P$_2'$ is quite distinct from those observed in the UV−vis (50 ns and 10 μs, Figure 2), lagging and preceding the former and the latter by a decade in time, respectively. The 50 ns component (formation of P$_2$) cannot represent ECN translocation into the N-terminal domain because the protein structural changes that would allow for it have not occurred yet. On that time scale, ECN is expected to remain close to its original binding pocket, but moving out of hydrogen bond distance with W288/Y201. In contrast, the 10 μs time process in the UV−vis TA data (formation of P$_3$) could well represent ECN translocation, as it reports on a significant change of ECN environment that is

similar to that of the OCP^R state, and the required NTD structural changes are completed by that time. Yet, the ECN translocation event cannot form the trigger for the N-terminal domain secondary structure changes given the temporal discrepancy. Obviously, breaking the hydrogen bonds between ECN and W288/Y201 in the C-terminal domain results in the N-terminal domain changes, but it is difficult to imagine how C-terminal domain changes propagate into the N-terminal domain through the protein backbone, as we have shown that the former are minimal. Instead, we note that even very small movements of the carotenoid will be sensed by the Y44 and W110 residues in the N-terminal domain, which interact with the ECN β2-ring via $\pi-\pi$ stacking interactions of their aromatic side chains (Figure 1B).[18,19] W110 and Y44 are in helices C and G, respectively, which are the two helices that were shown to move[11] (Figure 8A) and that also bind L37 (helix C) and M117 (helix G), which obstruct the carotenoid tunnel in OCP^O. Thus, formation of P$_2$ may correspond to rupture of the $\pi-\pi$ stacking interactions between the ECN β_2-ring and W110 and Y44, which may trigger the changes in the N-terminal domain helices in P$_2'$, which occur more slowly on the (sub)microsecond time scale.

On the basis of the above considerations and the close resemblance between P$_3$ and OCP^R, we propose that, in 10 μs, ECN translocates into the N-terminal domain, resulting in the P$_3$ product state. Subsequently, on time scales longer than 0.5 ms, the NTE and CTT helices unfold and/or dissociate from the C-terminal β-sheet, which allows domain separation to take place, generating OCP^R and enabling binding to the phycobilisome. This interpretation is consistent with our transient UV−vis results: P$_3$ has a slightly red-shifted zero-crossing with respect to OCP^R. If domain separation happens on a longer time scale, this will result in partial solvent
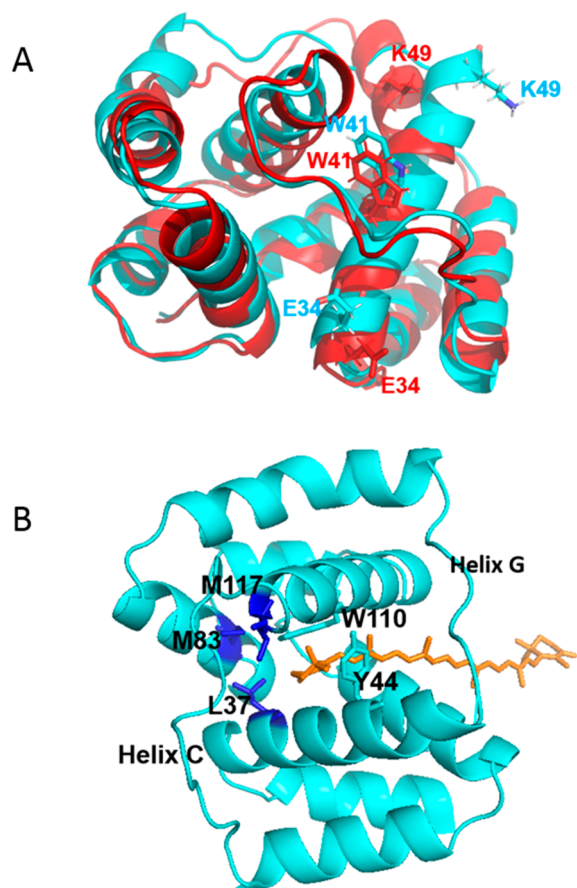
Figure 8. (A) Structure comparison between the NTD in OCP^O (cyan) and the isolated N-terminal domain (red). The figure shows the rotation of helix C with different position of three amino acids (E34, W41, K49). (B) The structure of the N-terminal domain in the OCP^O state (cyan) and ECN (orange), showing the carotenoid tunnel and the three amino acids (M117, M83, L37, in dark blue) forming the bottlenecks for carotenoid translocation. Y44 and W110, essential for photoactivation,[8,19] are placed in helices C and G, respectively. Small movement of the carotenoid may induce changes in the position of helices C and G through disruption of the π−π interactions between Y44/W110 and the ECN β2-ring. Replacement of W110 and/or Y44 by Ser abolishes photoactivation. By contrast, replacement by Phe does not hinder photoactivation,[19] suggesting that aromatic π−π interactions with the ECN β2-ring constitute a key element.

exposure of ECN, which could cause the remaining blue-shift of the ECN product to that of OCP^R.

■ CONCLUSIONS

We thoroughly assessed the OCP reaction mechanism from the femtosecond to submillisecond time scale by means of time-resolved electronic and vibrational spectroscopy, thereby identifying distinct photoproduct intermediates P$_1$, P$_2$, P$_2'$, and P$_3$. We propose a comprehensive reaction model where the β1-ring of the ECN carotenoid remains all-trans upon photo-activation and the hydrogen-bond rupture with conserved aromatic side chains at the ECN β1-ring initiates structural changes at the N-terminal domain in 0.5−1.1 μs, which allow the carotenoid to translocate into the N-terminal domain in 10 μs. These events precede the dissocation and unfolding of the NTE and CTT, which occur on time scales longer than 0.5 ms, by at least two decades of time.

■ MATERIALS AND METHODS

Construction of Plasmids Containing *Synechocystis* Wild-Type and Mutated OCP Genes for Expression in *Escherichia coli* and Holoprotein Production In Echinenone-Producing *E. coli*. The construction of plasmids containing the wild-type OCP gene (pCDF-NtagOCPSyn) and the mutated OCP ΔNTE gene (pCDF-Δ2−20 OCP-Ntag) with nucleotides coding for six histidines in the N-terminus were previously described in refs 60 and 63, respectively. To construct the plasmid pCDF-NtagOCPSyn-ΔCTT, the C-terminal tail (last 11 amino acids just before the stop codon) was deleted by mutagenesis using the plasmid pCDF-NtagOCPSyn[60] and the primers F-OCP-ΔCTT (5′-GGCAAAATTTTCTTT-GTGGCGATCGACTAGAATAACTCCCTTCAGAG-3′) and R-OCP-ΔCTT (5′- GTCGATCGCCACAAAGAAAATTTTG-CCCTCGGGGTTGAGGAG-3′). All plasmids were checked by sequencing.

BL21 (DE3) cells from Agilent Technologies were transformed simultaneously with three plasmids: (1) pACBETA, (2) pBAD-CrtO, and (3) pCDF-OCP (containing WT and mutated *ocp* genes). The construction of pACBETA and pBAD-CrtO plasmids was described by Bourcier de Carbon et al.[60] The *crtBEIY* operon in pACBETA was constitutively expressed under the control of the *crtE* promoter, whereas the *crtW* gene was under the control of the arabinose-inducible promoter araBAD and the *ocp* gene was under the control of a T7 RNA polymerase promoter and their expression was enhanced by addition of IPTG. The isolation of holo OCPs was described by Bourcier de Carbon et al.[60] Briefly, cells were resuspended in lysis buffer (40 mM Tris pH 8/10% glycerol/300 mM NaCl/1 mM EDTA/1 mM PMSF, 1 mM caproic acid/1 mM benzamidic acid/50 μg mL^{-1} DNase) and then broken in dim light using a French press. The membranes were pelleted and the supernatant was loaded on a nickel affinity column (Ni-Probond resin, Invitrogen). Proteins were eluted with 250 mM imidazole and then dialyzed against 40 mM Tris-HCl pH 8.

Light-Minus-Dark Difference FTIR Spectroscopy. Infrared difference spectra were recorded using an FTIR spectrometer (IFS 66s Bruker) equipped with a nitrogen-cooled photovoltaic MCT detector (20 MHz, KV 100, Kolmar Technologies) described earlier.[64] A blue LED emitting at 470 nm was used for photo-conversion at saturating intensity, and the wild-type sample was light-adapted several times before measurement. The sample was contained between CaF$_2$ windows separated with a 20 μm Teflon spacer for D$_2$O buffer and without a spacer for H$_2$O buffer and the concentration was tuned for OD ∼ 0.8 absorption at 1650 cm^{-1}.

Femto- to Submillisecond Mid-IR Transient Absorption Spectroscopy. Femtosecond to submillisecond transient mid-IR absorption measurements were performed on a setup described before,[65] extended with pulsed light originating from dual electroni-cally synchronized femtosecond regenerative amplifiers, yielding a controllable delay between the optical pump and mid-IR probe pulses.[28] The former was a 1 kHz Ti:sapphire amplifier (Hurricane, Spectra Physics) pumping an optical parametric amplifier (Topas C, Light Conversion) tuned to 475 nm output and attenuated to 2 μJ excitation energy at the sample position. To improve the efficiency of ECN singlet excitation and thereby enhance the signal at long time delays, the excitation pulse was deliberately chirped to ∼2 ps by transmission through a 10 cm SF11 glass rod. The probe laser was a 1 kHz Ti:sapphire amplifier (Spitfire Ace, Spectra Physics) that pumped a separate optical parametric amplifier (Topas, Light Conversion), producing signal and idler beams that underwent subsequent difference frequency generation in AgGaS$_2$, yielding femtosecond mid-IR pulses tunable from 1 to 10 μm center wavelength with ∼100 fs pulse duration. The pump and probe beams were spatially and temporally overlapped on the sample, and data were collected from 0 to 120 μs or to 585 μs distributed logarithmically with background spectra measured at negative time delay. The probe light was spectrally resolved and detected with a liquid-N$_2$-cooled 32-pixel MCT array (InfraRed Associates). Difference absorption data were calculated as the difference between probe spectrum with and without exposure to pump light which was modulated in situ by an optical

chopper wheel set to half the laser repetition rate. The sample was refreshed by scanning in a Lissajous pattern with a return time of 2 min. Polarization control for mid-IR TA and anisotropy measurements was achieved using a Berek's variable waveplate (Newport) set for $\lambda/2$ retardance at 475 nm and a wire-grid polarizer (Thorlabs). Anistropy measurements were carried out with an unstretched pump pulse at a delay of 2 ps between pump and probe.

Femto- to Submillisecond UV–Vis Transient Absorption Spectroscopy. Transient UV–vis absorption measurements were performed with a femtosecond-to-submillisecond pump–probe setup utilizing a pair of electronically synchronized Ti:sapphire amplified laser systems (Legend and Libra, Coherent) as reported previously.[66–69] A CaF$_2$ plate on a homemade moving stage was used for supercontinuum white light generation, which was focused and overlapped with the pump beam in the sample, after which the probe beam was spectrally dispersed and detected in a multichannel detection system (Entwicklungsburo Stresing) comprising a prism spectrograph and a 1024-pixel back-thinned FFT-CCD detector (S7030-1006, Hamamatsu). The time delay was varied up to 750 μs. The central wavelength and the power of the pump beam were set at 475 nm and 400 nJ, respectively. The instrument response function was ~100 fs.

Global Analysis Methodology. Global analysis fitting was performed for the transient absorption spectra using the Glotaran program.[31,32] With global analysis, all wavelengths were analyzed simultaneously with a set of common time constants. A kinetic model was applied consisting of sequentially interconverting, evolution-associated difference spectra (EADS), i.e., $1 \rightarrow 2 \rightarrow 3 \rightarrow ...$, in which the arrows indicate successive monoexponential decays of a time constant, which can be regarded as the lifetime of each EADS. The first EADS corresponds to the difference spectrum at time zero. The first EADS evolves into the second EADS with time constant τ_1, which in turn evolves into the third EADS with time constant τ_2, etc. The procedure clearly visualizes the evolution of the intermediate states of the protein.[51]

ASSOCIATED CONTENT

Ⓢ Supporting Information

The Supporting Information is available free of charge on the ACS Publications website at DOI: 10.1021/jacs.8b11373.

> UV–vis global analysis results; time-resolved raw and fitted UV–vis spectra; UV–vis absorption and absorption difference spectra; data set at lower excitation power; mid-IR kinetic traces and fits; transient concentration profiles, parallel reaction schemes, and species-associated difference spectra; mid-IR transient absorption spectrum of ECN in organic solvent; raw time-resolved mid-IR spectra on long time scales (PDF)

AUTHOR INFORMATION

Corresponding Author

*j.t.m.kennis@vu.nl

ORCID 🅾

John T. M. Kennis: 0000-0002-3563-2353

Notes

The authors declare no competing financial interest.

ACKNOWLEDGMENTS

REFERENCES

(1) Horton, P.; Ruban, A. V.; Walters, R. G. *Annu. Rev. Plant Physiol. Plant Mol. Biol.* **1996**, *47*, 655.

(2) Croce, R.; van Amerongen, H. *Nat. Chem. Biol.* **2014**, *10*, 492.

(3) Kirilovsky, D.; Kerfeld, C. A. *Nat. Plants* **2016**, *2*, 16180.

(4) Demmigadams, B. *Biochim. Biophys. Acta, Bioenerg.* **1990**, *1020*, 1.

(5) Horton, P.; Ruban, A. V.; Walters, R. G. *Plant Physiol.* **1994**, *106*, 415.

(6) Holt, T. K.; Krogmann, D. W. *Biochim. Biophys. Acta, Bioenerg.* **1981**, *637*, 408.

(7) Wilson, A.; Ajlani, G.; Verbavatz, J. M.; Vass, I.; Kerfeld, C. A.; Kirilovsky, D. *Plant Cell* **2006**, *18*, 992.

(8) Wilson, A.; Punginelli, C.; Gall, A.; Bonetti, C.; Alexandre, M.; Routaboul, J. M.; Kerfeld, C. A.; van Grondelle, R.; Robert, B.; Kennis, J. T. M.; Kirilovsky, D. *Proc. Natl. Acad. Sci. U. S. A.* **2008**, *105*, 12075.

(9) Wilson, A.; Gwizdala, M.; Mezzetti, A.; Alexandre, M.; Kerfeld, C. A.; Kirilovsky, D. *Plant Cell* **2012**, *24*, 1972.

(10) Liu, H. J.; Zhang, H.; King, J. D.; Wolf, N. R.; Prado, M.; Gross, M. L.; Blankenship, R. E. *Biochim. Biophys. Acta, Bioenerg.* **2014**, *1837*, 1955.

(11) Leverenz, R. L.; Sutter, M.; Wilson, A.; Gupta, S.; Thurotte, A.; Bourcier de Carbon, C.; Petzold, C. J.; Ralston, C.; Perreau, F.; Kirilovsky, D.; Kerfeld, C. A. *Science* **2015**, *348*, 1463.

(12) Gupta, S.; Guttman, M.; Leverenz, R. L.; Zhumadilova, K.; Pawlowski, E. G.; Petzold, C. J.; Lee, K. K.; Ralston, C. Y.; Kerfeld, C. A. *Proc. Natl. Acad. Sci. U. S. A.* **2015**, *112*, E5567.

(13) Liu, H. J.; Zhang, H.; Orf, G. S.; Lu, Y.; Jiang, J.; King, J. D.; Wolf, N. R.; Gross, M. L.; Blankenship, R. E. *Biochemistry* **2016**, *55*, 1003.

(14) Maksimov, E. G.; Sluchanko, N. N.; Mironov, K. S.; Shirshin, E. A.; Klementiev, K. E.; Tsoraev, G. V.; Moldenhauer, M.; Friedrich, T.; Los, D. A.; Allakhverdiev, S. I.; Paschenko, V. Z.; Rubin, A. B. *Biophys. J.* **2017**, *112*, 46.

(15) Maksimov, E. G.; Sluchanko, N. N.; Slonimskiy, Y. B.; Slutskaya, E. A.; Stepanov, A. V.; Argentova-Stevens, A. M.; Shirshin, E. A.; Tsoraev, G. V.; Klementiev, K. E.; Slatinskaya, O. V.; Lukashev, E. P.; Friedrich, T.; Paschenko, V. Z.; Rubin, A. B. *Sci. Rep.* **2017**, *7*, 15548.

(16) Tian, L. J.; van Stokkum, I. H. M.; Koehorst, R. B. M.; Jongerius, A.; Kirilovsky, D.; van Amerongen, H. *J. Am. Chem. Soc.* **2011**, *133*, 18304.

(17) van Stokkum, I. H. M.; Gwizdala, M.; Tian, L.; Snellenburg, J. J.; van Grondelle, R.; van Amerongen, H.; Berera, R. *Photosynth. Res.* **2018**, *135*, 87.

(18) Kerfeld, C. A.; Sawaya, M. R.; Brahmandam, V.; Cascio, D.; Ho, K. K.; Trevithick-Sutton, C. C.; Krogmann, D. W.; Yeates, T. O. *Structure* **2003**, *11*, 55.

(19) Wilson, A.; Kinney, J. N.; Zwart, P. H.; Punginelli, C.; D'Haene, S.; Perreau, F.; Klein, M. G.; Kirilovsky, D.; Kerfeld, C. A. *J. Biol. Chem.* **2010**, *285*, 18364.

(20) Harris, D.; Tal, O.; Jallet, D.; Wilson, A.; Kirilovsky, D.; Adir, N. *Proc. Natl. Acad. Sci. U. S. A.* **2016**, *113*, E1655.

(21) Harris, D.; Wilson, A.; Muzzopappa, F.; Sluchanko, N. N.; Friedrich, T.; Maksimov, E. G.; Kirilovsky, D.; Adir, N. *Nat. Comm. Biol.* **2018**, *1*, 125.

(22) Brust, R.; Lukacs, A.; Haigney, A.; Addison, K.; Gil, A.; Towrie, M.; Clark, I. P.; Greetham, G. M.; Tonge, P. J.; Meech, S. R. *J. Am. Chem. Soc.* **2013**, *135*, 16168.

(23) Laptenok, S. P.; Lukacs, A.; Gil, A.; Brust, R.; Sazanovich, I. V.; Greetham, G. M.; Tonge, P. J.; Meech, S. R. *Angew. Chem., Int. Ed.* **2015**, *54*, 9303.

(24) Gil, A. A.; Laptenok, S. P.; French, J. B.; Iuliano, J. N.; Lukacs, A.; Hall, C. R.; Sazanovich, I. V.; Greetham, G. M.; Bacher, A.; Illarionov, B.; Fischer, M.; Tonge, P. J.; Meech, S. R. *J. Phys. Chem. B* **2017**, *121*, 1010.

(25) Mathes, T.; Heilmann, M.; Pandit, A.; Zhu, J. Y.; Ravensbergen, J.; Kloz, M.; Fu, Y. A.; Smith, B. O.; Christie, J. M.; Jenkins, G. I.; Kennis, J. T. M. *J. Am. Chem. Soc.* **2015**, *137*, 8113.

(26) Hontani, Y.; Marazzi, M.; Stehfest, K.; Mathes, T.; van Stokkum, I. H. M.; Elstner, M.; Hegemann, P.; Kennis, J. T. M. *Sci. Rep.* **2017**, *7*, 7217.

(27) Hontani, Y.; Inoue, K.; Kloz, M.; Kato, Y.; Kandori, H.; Kennis, J. T. M. *Phys. Chem. Chem. Phys.* **2016**, *18*, 24729.

(28) Konold, P. E.; Mathes, T.; Weissenborn, J.; Groot, M. L.; Hegemann, P.; Kennis, J. T. M. *J. Phys. Chem. Lett.* **2016**, *7*, 3472.

(29) Mathes, T.; Ravensbergen, J.; Kloz, M.; Gleichmann, T.; Gallagher, K. D.; Woitowich, N. C.; St Peter, R.; Kovaleva, S. E.; Stojkovic, E. A.; Kennis, J. T. M. *J. Phys. Chem. Lett.* **2015**, *6*, 239.

(30) Zhu, J. Y.; Mathes, T.; Hontani, Y.; Alexandre, M. T. A.; Toh, K. C.; Hegemann, P.; Kennis, J. T. M. *J. Phys. Chem. Lett.* **2016**, *7*, 4380.

(31) Snellenburg, J. J.; Laptenok, S. P.; Seger, R.; Mullen, K. M.; van Stokkum, I. H. M. *J. Stat. Software* **2012**, *49*, DOI: 10.18637/jss.v049.i03

(32) van Stokkum, I. H. M.; Larsen, D. S.; van Grondelle, R. *Biochim. Biophys. Acta, Bioenerg.* **2004**, *1657*, 82.

(33) Polivka, T.; Kerfeld, C. A.; Pascher, T.; Sundstrom, V. *Biochemistry* **2005**, *44*, 3994.

(34) Slouf, V.; Kuznetsova, V.; Fuciman, M.; de Carbon, C. B.; Wilson, A.; Kirilovsky, D.; Polivka, T. *Photosynth. Res.* **2017**, *131*, 105.

(35) Polivka, T.; Sundstrom, V. *Chem. Phys. Lett.* **2009**, *477*, 1.

(36) Gradinaru, C. C.; Kennis, J. T. M.; Papagiannakis, E.; van Stokkum, I. H. M.; Cogdell, R. J.; Fleming, G. R.; Niederman, R. A.; van Grondelle, R. *Proc. Natl. Acad. Sci. U. S. A.* **2001**, *98*, 2364.

(37) Papagiannakis, E.; Kennis, J. T. M.; van Stokkum, I. H. M.; Cogdell, R. J.; van Grondelle, R. *Proc. Natl. Acad. Sci. U. S. A.* **2002**, *99*, 6017.

(38) Papagiannakis, E.; Das, S. K.; Gall, A.; van Stokkum, I. H. M.; Robert, B.; van Grondelle, R.; Frank, H. A.; Kennis, J. T. M. *J. Phys. Chem. B* **2003**, *107*, 5642.

(39) Wohlleben, W.; Buckup, T.; Herek, J. L.; Cogdell, R. J.; Motzkus, M. *Biophys. J.* **2003**, *85*, 442.

(40) Papagiannakis, E.; van Stokkum, I. H. M.; Vengris, M.; Cogdell, R. J.; van Grondelle, R.; Larsen, D. S. *J. Phys. Chem. B* **2006**, *110*, 5727.

(41) Liguori, N.; Xu, P. Q.; van Stokkum, I. H. M.; van Oort, B.; Lu, Y. H.; Karcher, D.; Bock, R.; Croce, R. *Nat. Commun.* **2017**, *8*, 1994.

(42) Kloz, M.; Weissenborn, J.; Polivka, T.; Frank, H. A.; Kennis, J. T. M. *Phys. Chem. Chem. Phys.* **2016**, *18*, 14619.

(43) Wohlleben, W.; Buckup, T.; Hashimoto, H.; Cogdell, R. J.; Herek, J. L.; Motzkus, M. *J. Phys. Chem. B* **2004**, *108*, 3320.

(44) Niedzwiedzki, D.; Koscielecki, J. F.; Cong, H.; Sullivan, J. O.; Gibson, G. N.; Birge, R. R.; Frank, H. A. *J. Phys. Chem. B* **2007**, *111*, 5984.

(45) Kodis, G.; Herrero, C.; Palacios, R.; Marino-Ochoa, E.; Gould, S.; de la Garza, L.; van Grondelle, R.; Gust, D.; Moore, T. A.; Moore, A. L.; Kennis, J. T. M. *J. Phys. Chem. B* **2004**, *108*, 414.

(46) Berera, R.; van Stokkum, I. H. M.; Kodis, G.; Keirstead, A. E.; Pillai, S.; Herrero, C.; Palacios, R. E.; Vengris, M.; van Grondelle, R.; Gust, D.; Moore, T. A.; Moore, A. L.; Kennis, J. T. M. *J. Phys. Chem. B* **2007**, *111*, 6868.

(47) Kish, E.; Pinto, M. M. M.; Kirilovsky, D.; Spezia, R.; Robert, B. *Biochim. Biophys. Acta, Bioenerg.* **2015**, *1847*, 1044.

(48) Fujisawa, T.; Leverenz, R. L.; Nagamine, M.; Kerfeld, C. A.; Unno, M. *J. Am. Chem. Soc.* **2017**, *139*, 10456.

(49) Ernst, O. P.; Lodowski, D. T.; Elstner, M.; Hegemann, P.; Brown, L. S.; Kandori, H. *Chem. Rev.* **2014**, *114*, 126.

(50) Kottke, T.; Xie, A. H.; Larsen, D. S.; Hoff, W. D. In *Annual Review of Biophysics*; Dill, K. A., Ed.; Annual Reviews: Palo Alto, CA, 2018; Vol. *47*, p 291.

(51) Kennis, J. T. M.; Groot, M. L. *Curr. Opin. Struct. Biol.* **2007**, *17*, 623.

(52) Toh, K. C.; Stojkovic, E. A.; van Stokkum, I. H. M.; Moffat, K.; Kennis, J. T. M. *Proc. Natl. Acad. Sci. U. S. A.* **2010**, *107*, 9170.

(53) Ihalainen, J. A.; Gustavsson, E.; Schroeder, L.; Donnini, S.; Lehtivuori, H.; Isaksson, L.; Thoing, C.; Modi, V.; Berntsson, O.; Stucki-Buchli, B.; Liukkonen, A.; Hakkanen, H.; Kalenius, E.; Westenhoff, S.; Kottke, T. *J. Am. Chem. Soc.* **2018**, *140*, 12396.

(54) Bandara, S.; Ren, Z.; Lu, L.; Zeng, X. L.; Shin, H.; Zhao, K. H.; Yang, X. *J. Proc. Natl. Acad. Sci. U. S. A.* **2017**, *114*, 6286.

(55) Yang, Y.; Linke, M.; von Haimberger, T.; Hahn, J.; Matute, R.; Gonzalez, L.; Schmieder, P.; Heyne, K. *J. Am. Chem. Soc.* **2012**, *134*, 1408.

(56) Alexandre, M. T. A.; Domratcheva, T.; Bonetti, C.; van Wilderen, L.; van Grondelle, R.; Groot, M. L.; Hellingwerf, K. J.; Kennis, J. T. M. *Biophys. J.* **2009**, *97*, 227.

(57) Lakowicz, J. R. *Principles of Fluorescence Spectroscopy*, 3rd ed.; Springer, 2006.

(58) Berera, R.; van Stokkum, I. H. M.; Gwizdala, M.; Wilson, A.; Kirilovsky, D.; van Grondelle, R. *J. Phys. Chem. B* **2012**, *116*, 2568.

(59) Polivka, T.; Sundstrom, V. *Chem. Rev.* **2004**, *104*, 2021.

(60) Bourcier de Carbon, C.; Thurotte, A.; Wilson, A.; Perreau, F.; Kirilovsky, D. *Sci. Rep.* **2015**, *5*, 9085.

(61) Zayner, J. P.; Antoniou, C.; Sosnick, T. R. *J. Mol. Biol.* **2012**, *419*, 61.

(62) Blout, E. R.; Deloze, C.; Asadourian, A. *J. Am. Chem. Soc.* **1961**, *83*, 1895.

(63) Thurotte, A.; Lopez-Igual, R.; Wilson, A.; Comolet, L.; Bourcier de Carbon, C.; Xiao, F. G.; Kirilovsky, D. *Plant Physiol.* **2015**, *169*, 737.

(64) Alexandre, M. T. A.; van Grondelle, R.; Hellingwerf, K. J.; Kennis, J. T. M. *Biophys. J.* **2009**, *97*, 238.

(65) Groot, M. L.; van Wilderen, L. J. G. W.; Di Donato, M. *Photochem. Photobiol. Sci.* **2007**, *6*, 501.

(66) Ravensbergen, J.; Abdi, F. F.; van Santen, J. H.; Frese, R. N.; Dam, B.; van de Krol, R.; Kennis, J. T. M. *J. Phys. Chem. C* **2014**, *118*, 27793.

(67) Hontani, Y.; Inoue, K.; Kloz, M.; Kato, Y.; Kandori, H.; Kennis, J. T. *Phys. Chem. Chem. Phys.* **2016**, *18*, 24729.

(68) Hontani, Y.; Marazzi, M.; Stehfest, K.; Mathes, T.; van Stokkum, I. H. M.; Elstner, M.; Hegemann, P.; Kennis, J. T. M. *Sci. Rep.* **2017**, *7*, 7217.

(69) Berera, R.; van Grondelle, R.; Kennis, J. T. M. *Photosynth. Res.* **2009**, *101*, 105.